Astron. Astrophys. 164, 193–207 (1986)

ASTRONOMY AND ASTROPHYSICS

The structure and dynamics of evolved supernova remnants. The IC 443 complex

R. Braun[1,*] **and R. G. Strom**[2]

[1] Sterrewacht Leiden, Postbus 9513, 2300 RA Leiden, The Netherlands
[2] Netherlands Foundation for Radio Astronomy, Postbus 2, 7990 AA Dwingeloo, The Netherlands

Received January 2, accepted March 7, 1986

Summary. The extended cloud complex containing the supernova remnant IC 443, the H II region S 249 and members of the Gem OB1 association is studied with IRAS observations at 12, 25, 60 and 100 μm and WSRT observations at 327 and 1400 MHz and in the λ21 cm H I line.

IC 443 is shown to consist of three interconnected ~ spherical subshells of vastly different radii and centroids. The geometry is fully constrained by the structural and kinematic data. Two of these subshells together define the usually assumed boundaries of IC 443, while the third includes the optical filaments which extend beyond the bright north-eastern rim. These filaments are shown to have well correlated non-thermal radio counterparts.

Physical parameters are derived for the entire complex, individual H II regions and the shocked and recombined gas within IC 443 from the radio and infrared data. The available evidence implies that the SNR shock has encountered a pre-existing high density shell. It is shown that the system of subshells is fully consistent with formation by stellar wind driven bubbles generated by association members within the inhomogeneous environment of the complex.

Key words: Supernova remnants – IC 443 – H II regions – dust – bubbles – stellar winds

1. Introduction

IC 443 has long been considered a classic example of an evolved supernova remnant (SNR), and as such has received study in most accessible portions of the electromagnetic spectrum. Even so, our understanding of this source is less than satisfactory. Each additional observation appears to reveal a perplexing new component (with apparently distinct density, temperature and pressure) which must be reconciled with all those previously observed.

We attempt to synthesize a coherent analysis of IC 443 and its immediate surroundings from existing X-ray, optical and molecular line data as well as new data obtained with IRAS at 12, 25, 60, and 100 μm and the Westerbork Synthesis Radio Telescope (WSRT) at 1400 and 327 MHz and in the λ21 cm line of neutral hydrogen. We first discuss the observations and data reduction procedures in Sect. 2. In Sect. 3.1 we consider what conclusions can be drawn from the brightness distribution in the various wavelength bands, while in Sect. 3.2 we discuss the important physical processes and parameters which apply to the various components. General conclusions are summarized in Sect. 4, while specific conclusions and quantities can be found in the discussion of Sect. 3.

Send offprint requests to: R. Braun

* Now at National Radio Astronomy Observatory, PO Box 0, Socorro, NM 87801, USA

2. Observations and data reduction

2.1. Infrared data

The IC 443 region was observed in four infrared bands as part of the IRAS all sky survey (IRAS, 1985). Calibrated data obtained with the survey instrument detector array at 12, 25, 60, and 100 μm was gridded and co-added using standard software. Since the calibration history of this data is still poorly documented, the relative calibration with respect to the IRAS Skyflux (HCON 3) final product was determined by plotting the corresponding brightnesses at a similar resolution from identical grids covering a smoothly varying test field. The well-defined linear relationship had slope (CRDD/Skyflux) (1.3 ± 0.1; 1.6 ± 0.3; 1.4 ± 0.1; 1.4 ± 0.1) in the 12, 25, 60, and 100 μm bands respectively. This is consistent with a constant linear scaling with factor 0.71 ± 0.05 to obtain Skyflux surface brightnesses from CRDD data in each band. This factor has been applied to the data for the sake of consistency with the IRAS final products. The response to two bright foreground stars (AGK 3 +22 665 and +22 693) was masked out of the 12 and 25 μm images to prevent degradation of a larger map area during subsequent processing. The spatial frequency content of the data was then reorganized using the method of Braun (1986) to obtain an identical elliptical Gaussian (6.'9 × 4.'6, E-W × N-S) instrumental response in each of the four bands. The data from the second and third independent sky coverages (HCON 2 and HCON 3) was then combined to give the maps shown in Fig. 1. The effects of detector hysteresis should be minimal over this field since the satellite scan path (approximately between the ecliptic poles) does not encounter regions of excessively high surface brightness.

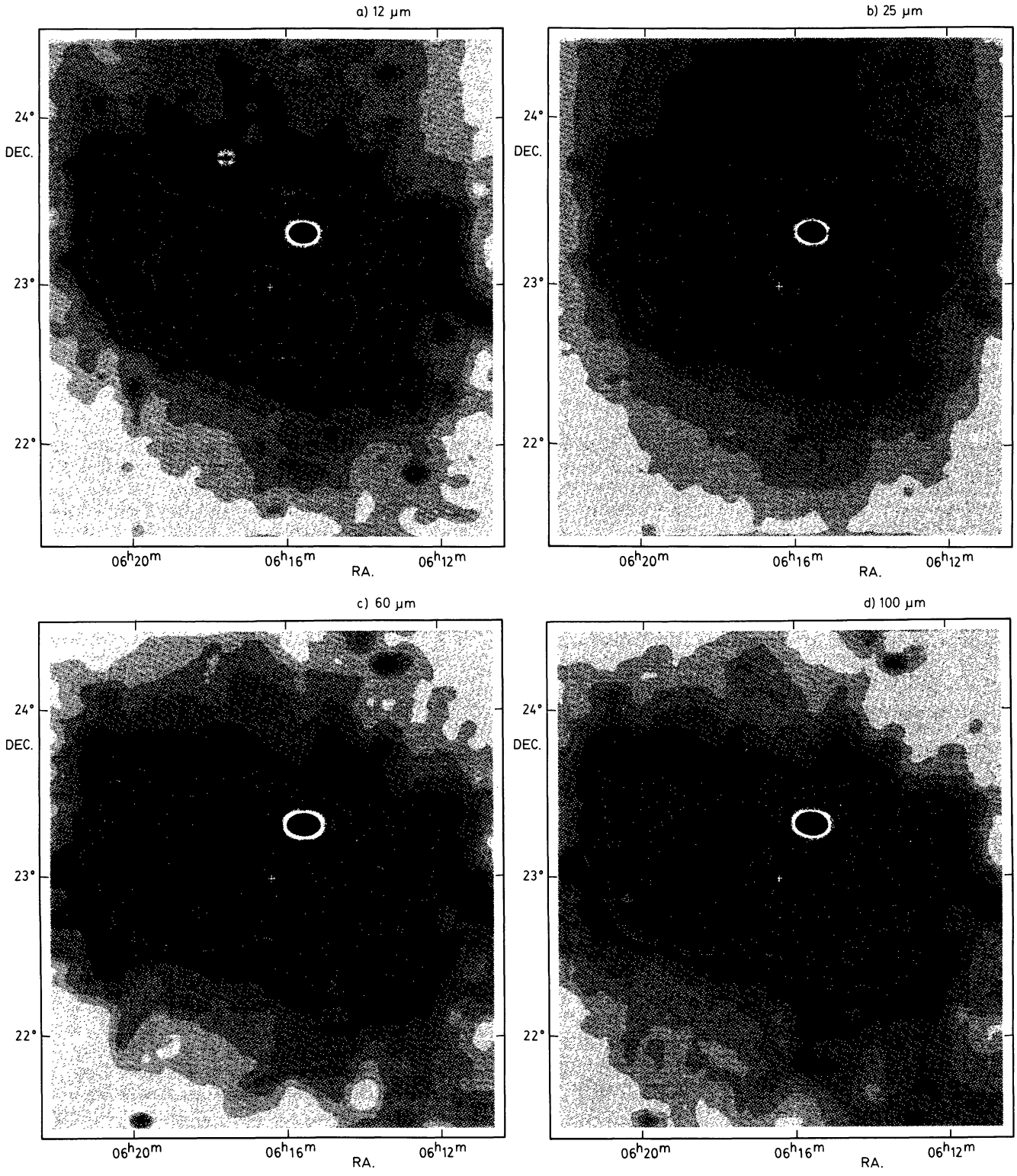

Fig. 1a–d. Dust emission from the IC 443 complex as observed in the 12, 25, 60, and 100 μm bands of IRAS. The beam in all four bands is an elliptical Gaussian 6.′9 × 4.′6 E-W × N-S). The grey scale in each map is based on a histogram of map intensities. Contours are in units of nominal surface brightness. **a** 12 μm image. The linear contour levels are 2.5 to 7.2 MJy/sr in steps of 0.36 MJy/sr. **b** 25 μm image. The linear contour levels are 4.5 to 11.3 MJy/sr in steps of 0.57 MJy/sr. **c** 60 μm image. The linear contour levels are 7.0 to 47.0 MJy/sr in steps of 2.5 MJy/sr. **d** 100 μm image. The linear contour levels are 25.6 to 128.0 MJy/sr in steps of 6.4 MJy/sr

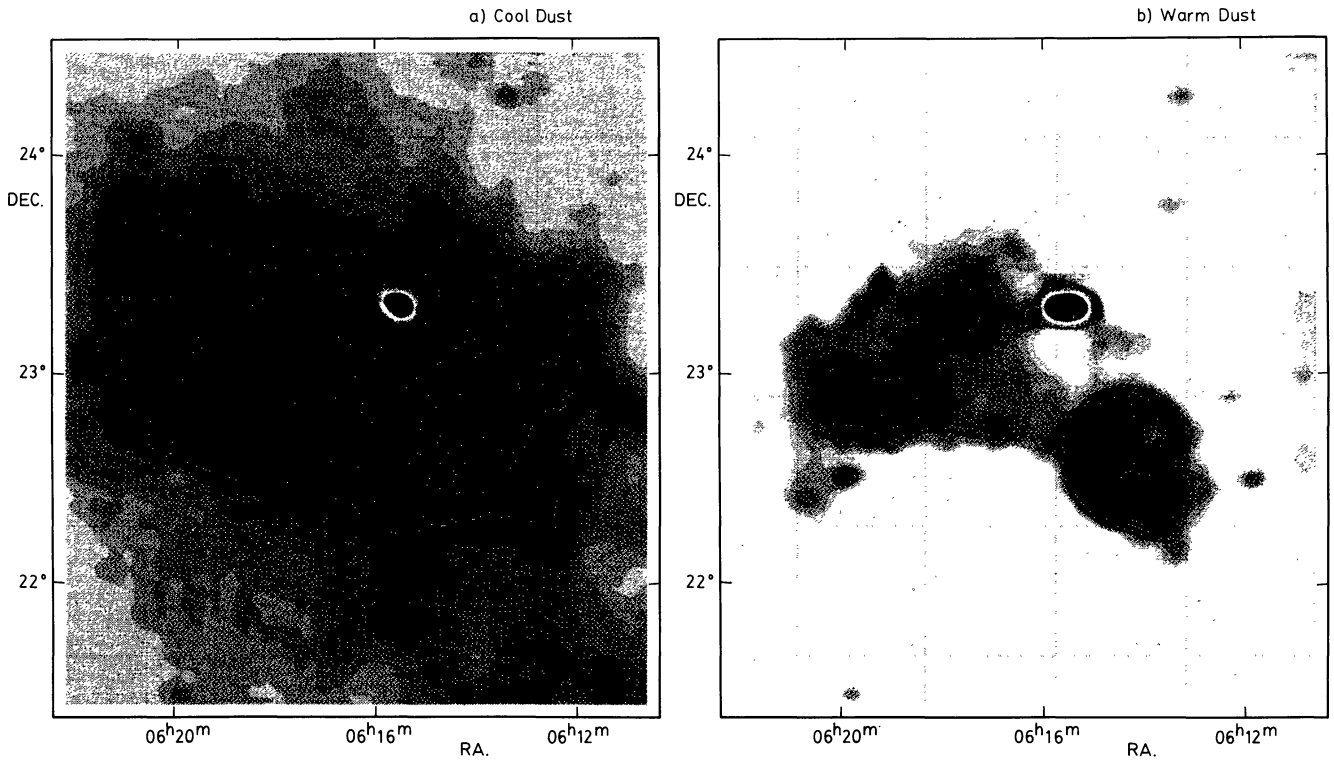

Fig. 2a and b. Cool and warm dust emission components derived from the maps in Fig. 1 by a three-component spectral decomposition. The grey scale is based on a histogram of map intensities. Contours are in units of nominal surface brightness in the 100 μm band. **a** Cool dust component. The linear contour levels are 25.6 to 128.0 MJy/sr in steps of 6.4 MJy/sr. **b** Warm dust component. The linear contour levels are 0.60 to 46.5 MJy/sr in steps of 5.1 MJy/sr

A spectral decomposition was used to model the data as a linear combination of cool dust, zodiacal light and warm dust emission (as discussed by Braun, 1986). Initial estimates of the four point component spectra made from the maps in Fig. 1 were iteratively adjusted to obtain uncorrelated component maps, optimized for the vicinity of IC 443. The cool (nominal brightness ratios at 12:25:60:100 μm = 0.040:0.040:0.226:1.000) and warm (nominal brightness ratios = 0.021:0.038:0.680:1.000) components which were so isolated are shown in Fig. 2. The decomposition has clearly been effective in separating these two components with the exception of the bright source at $\alpha = 6^h15^m30^s$, $\delta = 23°22'$ (these and all other positions are given for the epoch 1950.0) for which the decomposition was not well-tuned. The images of Fig. 1 were background corrected by subtracting appropriately scaled versions of both the cool dust component and a smoothly varying second order surface fit to the zodiacal light component (nominal brightness ratios = 0.44:1.00:0.48:0.19) from each. The resulting maps are shown in Fig. 3.

Integrated fluxes were derived for IC 443 via a box integration technique and are listed in Table 1. This was done by summing the images of Fig. 3 within rectangular boxes of increasing dimensions centered at $\alpha = 6^h14^m30^s$, $\delta = 22°30'$ so as to remove the effects of any remaining background offset over the source area (cf. Braun, 1986).

2.2. *Radio continuum data*

Radio continuum observations of IC 443 were made with the Westerbork Synthesis Radio Telescope (WSRT) at 1400 and 327 MHz during 1984 and 1985. The 1400 MHz field (36′ to half power) was centered on the relatively faint optical filaments to the north-east of the bright north-eastern radio/optical rim. The observation was a 4 × 12 h synthesis, providing regular sampling of the east-west baselines 36 to 2754 m with an 18 m increment. The digital continuum backend (DCB) was used to simultaneously observe eight bands of 5 MHz width in two orthogonal linear polarizations. Five of the eight bands in three contiguous groups were interference free on all observed baselines. Standard calibration sources and procedures were employed (Bos et al., 1981) to yield an absolute intensity accuracy of ~5% and a positional uncertainty ~0″.5. To avoid bandwidth smearing, the maps and synthesized antenna patterns at the three useful frequencies were individually generated and then combined in the map plane. A Gaussian taper, decreasing to 3% on the longest observed baseline was used to diminish near-in sidelobes. The low declination of IC 443 resulted in shadowing on some baselines which necessitated some form of deconvolution. The total intensity map (Stoke's parameter I) was first CLEAN'ed with a low loop gain and thereafter the method of Braun and Walterbos (1985) was employed to remove the remaining "short spacing bowl". The resulting image is shown in Fig. 4. Background variations caused by self-confusion in the field at a level of ~0.5 mJy/beam limit the sensitivity of the observation rather than the ~0.05 mJy/beam thermal noise.

The large field of view at 327 MHz (2°.7 to half power) allowed mapping of the entire infrared/optical complex. A 4 × 12 h synthesis ($B = 36 \rightarrow 2754$ m, $\Delta B = 18$ m) was obtained to provide a large, confusion free field (first grating "radius" at 2°.9 in R.A.). The digital line backend (DLB) was used to provide a 2.5 MHz total bandwidth in two orthogonal linear polarizations. After

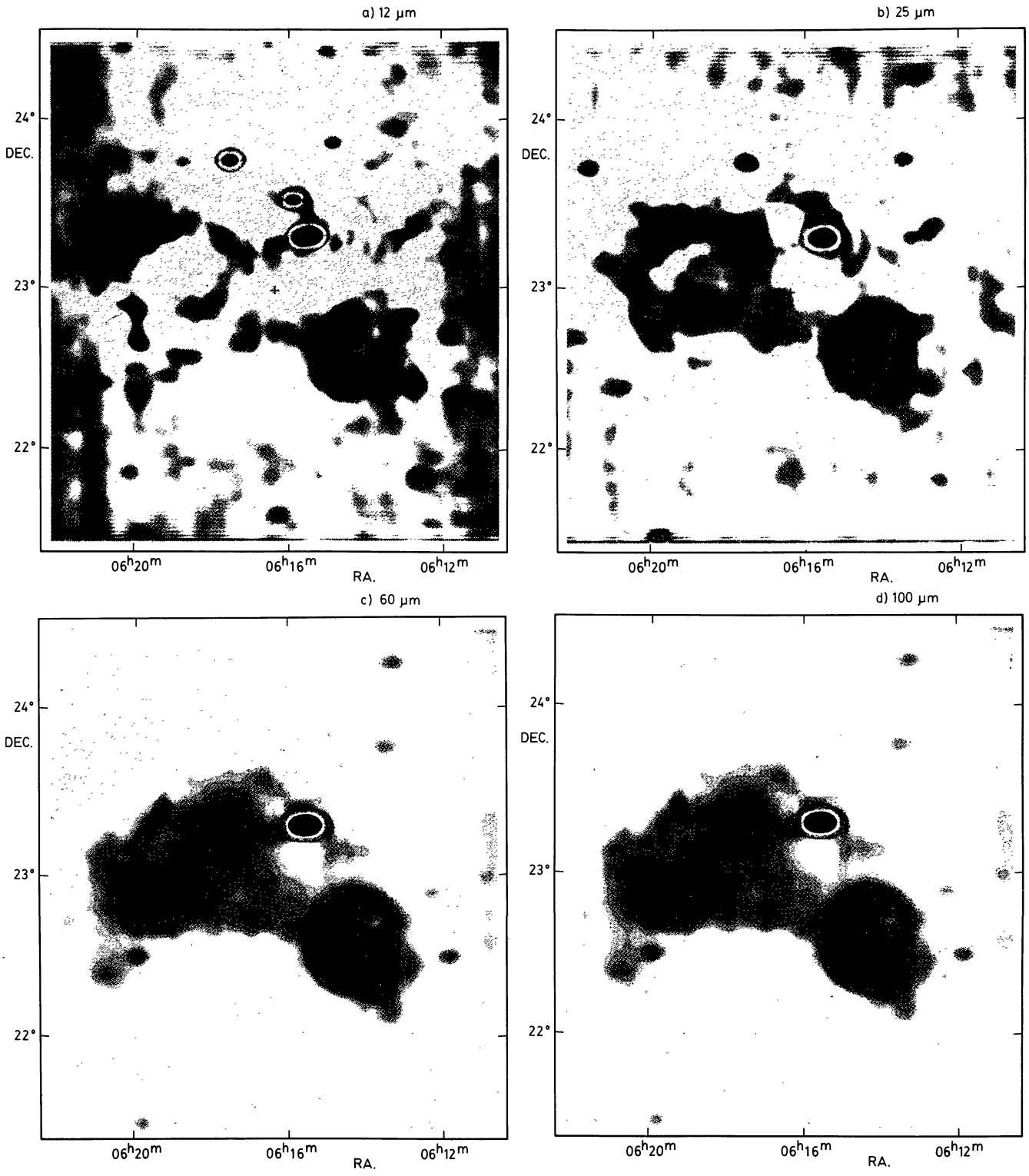

Fig. 3a–d. Background corrected warm dust emission from the IC 443 complex in the IRAS 12, 25, 60 and 100 μm bands. The maps are those of Fig. 1 after subtraction of the scaled cool dust component (Fig. 2a) and a second order surface fit to the zodiacal light component. The grey scale is based on a histogram of map intensities, excluding the faintest map areas. Contours are in units of nominal surface brightness. **a** 12 μm image. The linear contour levels are 0.53 to 1.79 MJy/sr in steps of 0.18 MJy/sr. **b** 25 μm image. The linear contour levels are 0.64 to 4.8 MJy/sr in steps of 0.32 MJy/sr. **c** 60 μm image. The linear contour levels are at 3.4 to 34.0 MJy/sr in steps of 3.4 MJy/sr. **d** 100 μm image. The linear contour levels are at 5.1 to 51.0 MJy/sr in steps of 5.1 MJy/sr

Table 1. Infrared spectral parameters for subshell *A* of IC 443

		Total	Shock-heated	Recombined
Nominal flux density [Jy]	(12 μm)	63.0 ± 6.0	( )	( )
	(25 μm)	85.0 ± 9.0	81.0 ± 12.0	4.0 ± 1.0
	(60 μm)	1260 ± 130	77.0 ± 12.0	1190 ± 180
	(100 μm)	1860 ± 190	19.0 ± 3.0	1840 ± 280
Color corrected flux [Jy]	(12 μm)		( )	( )
	(25 μm)		93.0 ± 14.0	4.0 ± 1.0
	(60 μm)		63.0 ± 9.0	1310 ± 200
	(100 μm)		17.0 ± 3.0	1860 ± 280
Color corrected λI_λ [$W\,m^{-2}\,sr^{-1}$]	(12 μm)		( )	( )
	(25 μm)		$2.4 \pm 0.4\ 10^{-7}$	$0.91 \pm 0.14\ 10^{-8}$
	(60 μm)		$6.7 \pm 1.0\ 10^{-8}$	$1.4 \pm 0.2\ 10^{-6}$
	(100 μm)		$1.1 \pm 0.2\ 10^{-8}$	$1.2 \pm 0.2\ 10^{-6}$
λ_{peak} [μm]			27.5 ± 1.0	
λI_λ^{max} [$W\,m^{-2}\,sr^{-1}$]			$2.5 \pm 0.4\ 10^{-7}$	
Angular radius [arcmin]		13.2		
Radius [pc]		5.8		
Distance [kpc]		1.5		

( ) Not defined by decomposition procedure

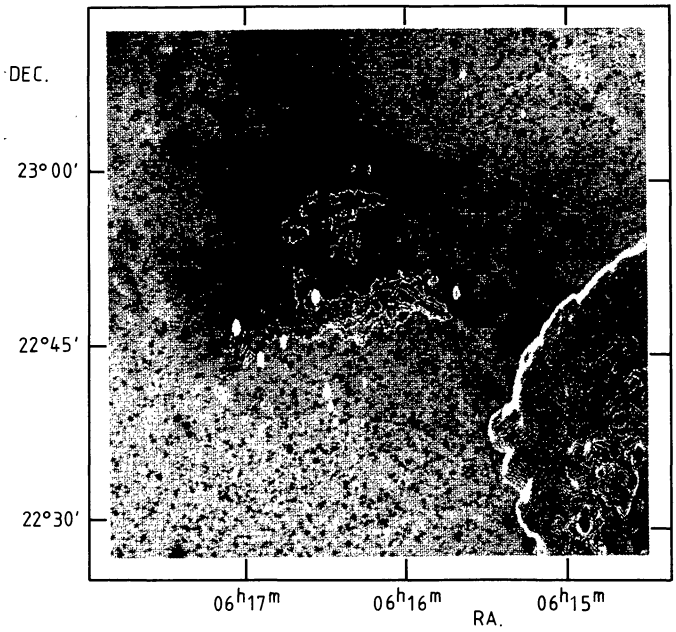

Fig. 4. Nonthermal radio counterparts to the north-eastern optical filaments. Contours of λ21 cm emission are overlaid on the digitized POSS E plate. The contour levels increase logarithmically by a factor 1.3 from the lowest contour level 1.154 mJy/beam (the 17″ × 43″ beam has solid angle $1.76\ 10^{-8}$ sr). The radio map is not corrected for the primary beam attenuation

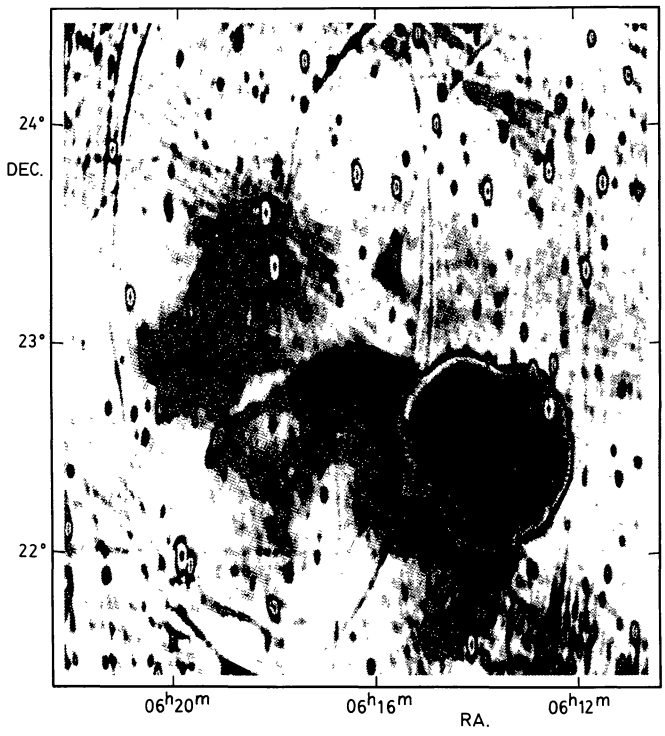

Fig. 5. Radio continuum emission from the IC 443 complex at 327 MHz. Contour and gray-scale transitions increase logarithmically by a factor of 1.3 from the lowest contour level 8.50 mJy/beam (the 72″ × 185″ beam has a solid angle $3.40\ 10^{-7}$ sr). A phase calibration error gives rise to residual rings (43.′4 × 111.′0) at the 0.2% level (before primary beam correction) around compact field sources and near $\alpha = 6^h12^m30^s$, $\delta = 21°40'$ due to the bright northeast rim of IC 443

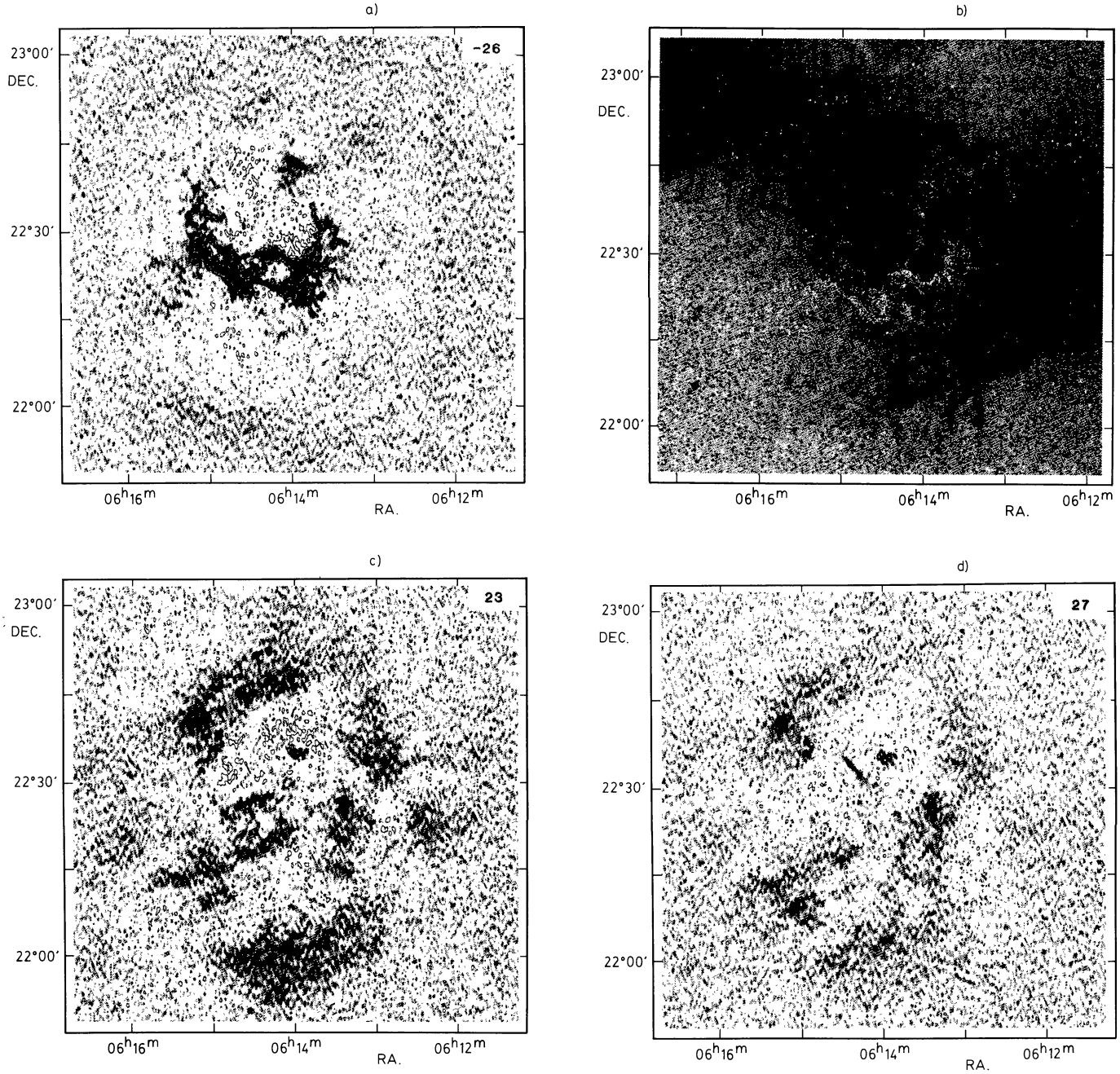

Fig. 6a–d. Accelerated recombined gas in IC 443. Channel maps of neutral hydrogen emission ($\Delta\alpha \times \Delta\delta \times \Delta v = 21'' \times 56'' \times 8.2\,\mathrm{km\,s^{-1}}$). The velocity of the band center is indicated at upper right of a, c and d. Contours are drawn for $T_B = \pm 2, 5, 10$, and 20 K. The maps are not corrected for primary beam attenuation. **a** Channel map at $V_{\mathrm{lsr}} = -26\,\mathrm{km\,s^{-1}}$. **b** The contours of the $V_{\mathrm{lsr}} = -26\,\mathrm{km\,s^{-1}}$ channel map overlaid on the digitized POSS E plate. **c** Channel map at $V_{\mathrm{lsr}} = -+23\,\mathrm{km\,s^{-1}}$. **d** Channel map at $V_{\mathrm{lsr}} = +27\,\mathrm{km\,s^{-1}}$

standard calibration and mapping, the total intensity map was CLEAN'ed, short spacing processed (Braun and Walterbos, 1985) and primary beam corrected, yielding the map of Fig. 5. Residual rings (43′.4 × 111′.) due to a phase calibration error are visible at the 0.2% level associated with the brightest field sources and in the extreme south-western portion of the field due to the north-east rim of IC 443 itself. At a still fainter level, ionospheric "spokes" can be seen radiating from bright compact sources. With the exception of the aforementioned localized artifacts, the emission is well represented.

In order to determine the spectral index of both the bright north-eastern rim of IC 443 and the filaments extending beyond this rim to the north-east, the 1400 MHz image was smoothed to the resolution of the 327 MHz map, while the primary beam corrected 327 MHz map was interpolated onto the same grid and tapered with the 1400 MHz primary beam. The spectral index was obtained for a number of subregions of the rim and filaments by determining the slope of temperature-temperature plots. The spectral index ($S \propto \nu^{-\alpha}$) determined in this way for the bright north-eastern rim of IC443 was $\alpha = 0.35 \pm 0.03$, while for the

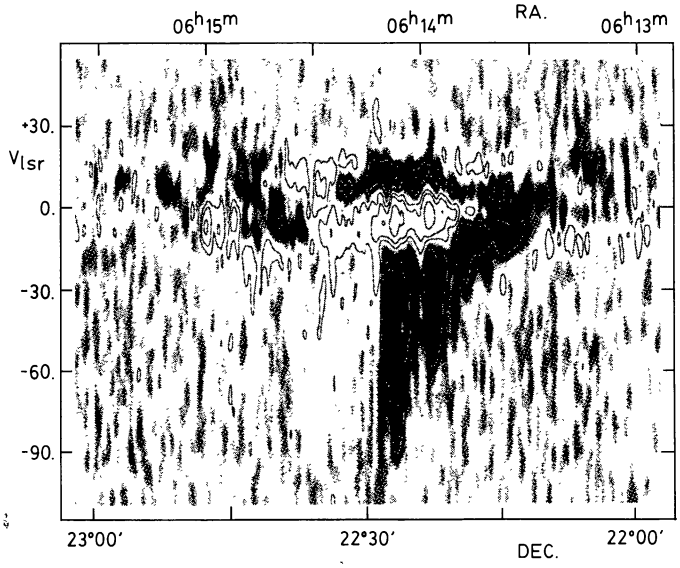

Fig. 7. Position-velocity structure of the neutral hydrogen. Cross-section through $\alpha = 6^h14^m16^s$, $\delta = 22°30'14''$ at position angle $\phi = 225$ for velocities between $V_{lsr} = -105$ and $+56\,km\,s^{-1}$. Contours are drawn for $T_B = \pm 2, \pm 5, \pm 10$ and 20 K

external filaments, $\alpha = 0.42 \pm 0.09$. Both of these values are clearly non-thermal, not significantly different and in good agreement with the value found by Erickson and Mahoney (1985) from integrated fluxes between 20 MHz and 11 GHz, $\alpha = 0.355 \pm 0.013$.

2.3. *Neutral hydrogen line data*

Observations of IC 443 in the $\lambda 21$ cm line of neutral hydrogen were carried out with the WSRT during 1982. A $250\,km\,s^{-1}$ band centered at $V_{lsr} = -10\,km\,s^{-1}$ was observed with resolution $\Delta\alpha \times \Delta\delta \times \Delta v = 21'' \times 56'' \times 8.2\,km\,s^{-1}$. The observations and data reduction techniques are discussed by Braun and Strom (1986a) who present the data in the form of channel maps between $V_{lsr} = -105$ and $+56\,km\,s^{-1}$ at $4.1\,km\,s^{-1}$ intervals. This was the range over which significant H I emission was detected with an r.m.s. sensitivity of $\Delta T_B = 0.61$ K. The emission at negative velocities is dominated by an incomplete semi-circular arc which is coincident with radio continuum filaments in the east-central portion of the SNR. This structure is illustrated by the channel map at $V_{lsr} = -2.6\,km\,s^{-1}$ shown in Fig. 6a and superposed on the (Leiden Astroscan) digitized POSS E plate in Fig. 6b. At positive velocities the bright north-eastern rim is seen (Fig. 6c) as well as extended emission in the south and south-east and long nearly linear features extending from the north-east to the south (Fig. 6d). A radial cross-section through the geometrical center of the arc $\alpha = 6^h14^m16^s$, $\delta = 22°30'14''$ at a position angle $\phi = 225°$ (shown in Fig. 7) illustrates the trend for observing larger radial velocities towards the center of this subshell. A compact cloud slightly south of the center of this subshell is observed to have both the highest radial velocities as well as the clearest indication for a phenomenon frequently observed in other clouds: a gradual shift in position of emission features with velocity. This pattern is illustrated by the series of mini channel maps of this cloud in Fig. 8a and the position-velocity diagram through the cloud center at fixed declination in Fig. 8b.

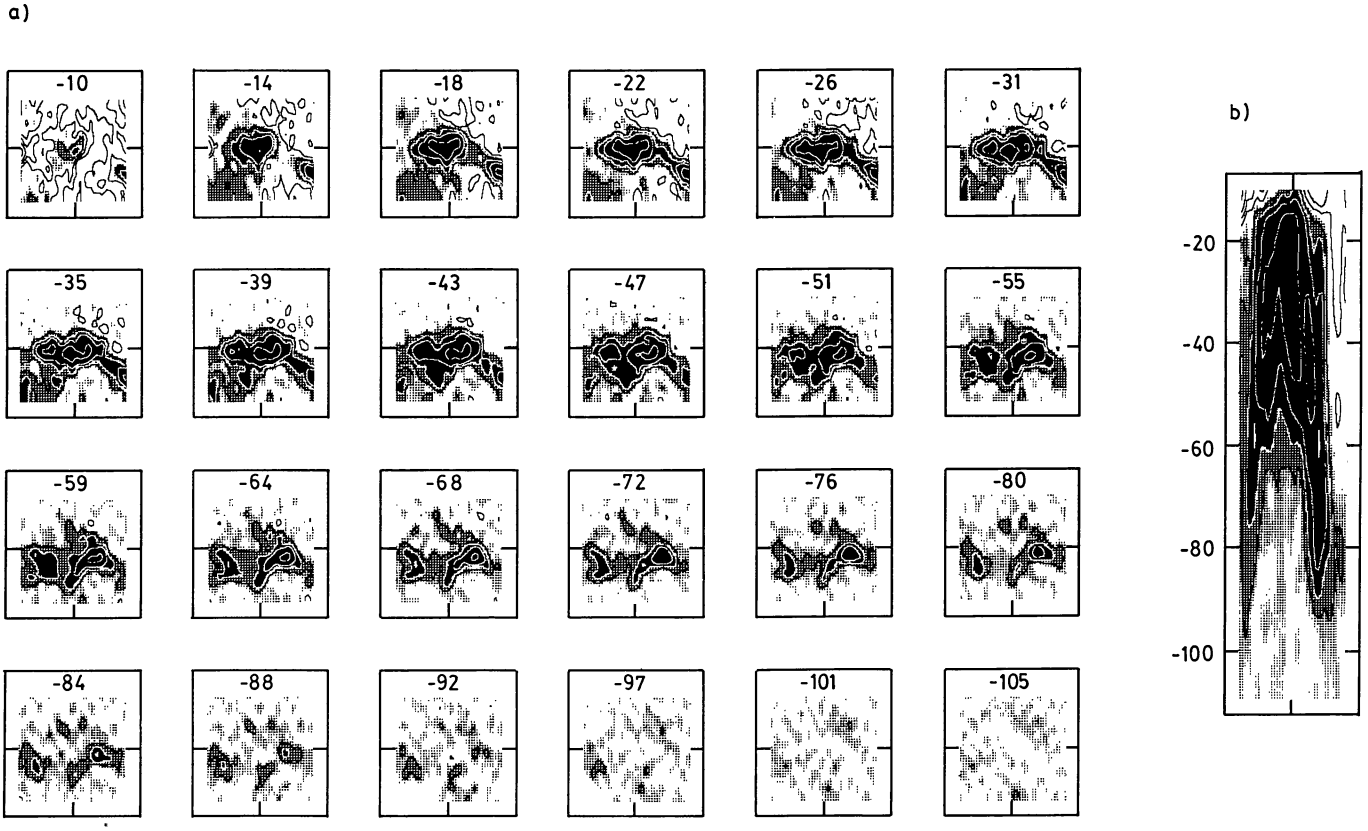

Fig. 8a and b. Velocity structure in a compact neutral cloud. Channel maps and $\alpha - V$ cut for a 7.2 arcmin field centered at $\alpha = 6^h14^m15^s$, $\delta = 22°27'$. Contours are drawn for $T_B = \pm 2, \pm 5, 10$ and 20 K. **a** Channel maps at velocities between $V_{lsr} = -10$ and $-105\,km\,s^{-1}$ as indicated. **b** Right ascension – velocity map at $\delta = 22°27'$ for velocities between $V_{lsr} = -10$ and $-105\,km\,s^{-1}$

3. Discussion

3.1. *Brightness distribution*

The cloud complex containing IC 443 ($l = 187°$ to $190°$ and $n = 2°$ to 5°5) is perhaps best seen in the distribution of cool dust shown in Fig. 2a. The edges of the complex are well-defined although at a lower level the system is connected to a more extensive cloud between $l = 188°$ to $198°$ and $b = -4°$ to $+2°$ shown in the 100 μm IRAS image (the composite of ~20 Spline I maps (Van Albada et al., 1984) projected onto galactic coordinates) in Fig. 9. Distance estimates to H II regions and their exciting stars in both complexes are similar, $D = 1.5 \pm 0.2$ kpc and especially in the case of the Gem OB1 association ($l = 187°$ to $191°$, $b = -2°$ to $+4°$), well-determined (eg. Humphreys, 1978; Israel, 1976) suggesting that the entire anticenter complex is physically associated. (Throughout the remainder of this paper we will assume $D = 1.5$ kpc.) The cool dust distribution of the IC 443 complex suggests an outer skeleton which has been consumed from within by the action of the massive stars of the Gem OB1 association. This is reflected in the central concentration of the warm dust seen in Fig. 2b. The warm peak at $\alpha = 6^h20^m$, $\delta = 22°53'$ is coincident with the O9 Vp star HD 256035 which is likely responsible for local heating and ionization, while other Gem OB1 members are seen (with similar distance moduli) throughout the complex. The brightest, best-studied members (following Humphreys, 1978) are marked in Fig. 10a and b on portions of the POSS E and O plates (digitized with the Leiden Observatory Astroscan) and listed in Table 2. Two bright foreground stars are visible on the western and eastern edges of the complex at $\alpha = 6^h12^m$ and $\alpha = 6^h20^m$, near $\delta = 23°5$. The bright, blue nebulosity in the central portion of the field is predominatnly scattered light from local association members (most probably HD 43753, B0.5 III and HD 43818, B0 II), while the diffuse photo-ionized gas is concentrated in the eastern half of the complex.

The filamentary shell of IC 443 is seen in the south-west, although the filaments extending beyond the shell at $\alpha = 6^h15^m$, $\delta = 22°45'$ to the north-east also appear to be collisionally ionized (Fesen, 1984). These north-eastern filaments correlate well with radio continuum counterparts as seen in the λ21 cm map of Fig. 4. This trend is also seen in other portions of IC 443 (cf. Duin and Van der Laan, 1975). The radio spectral index we determine from our data at 327 and 1400 MHz, $\alpha = 0.42 \pm 0.09$ is definitely non-thermal and consistent with that of the bright adjacent radio rim $\alpha = 0.35 \pm 0.03$. To the south of these filaments there is a rather abrupt change in the character of the diffuse optical nebulosity which seems suggestive of a change in the scattering geometry and/or grain density. A further indication for peculiar geometry is given by the filaments extending beyond the southern shell periphery at $\alpha = 6^h13^m30^s$, $\delta = 22°$ and lack of any obvious shell in the south-east.

The same complex has been recognized in neutral hydrogen surveys at a velocity $V_{lsr} = -5\,\mathrm{km\,s^{-1}}$ (e.g. Locke et al., 1964; DeNoyer, 1977), although its extent and brightness are somewhat confused by velocity crowding along the line of sight. High resolution H I studies (most recently that of Braun and Strom, 1986a) have given some insight into the geometry of the SNR. At velocities between $-5\,\mathrm{km\,s^{-1}}$ and $-100\,\mathrm{km\,s^{-1}}$ a semi-circular arc of accelerated post-shock gas (Fig. 6a) is seen coincident with the warm dust subshell of Fig. 2b centered at $\sim\alpha = 6^h14^m15^s$, $\delta = 22°35'$ with dimensions $25' \times 35'$. While this front-face subshell is coincident with the eastern optical rim (Fig. 6b) it does not extend south beyond $\delta = 22°20'$ and its western rim passes across the apparent center of IC 443. The SNR therefore appears to consist of at least two connected roughly spherical segments: the front face subshell (A) and a larger component centered at $\alpha = 6^h13^m15^s$, $\delta = 22°25'$ with dimensions $35' \times 50'$ (subshell B). It is also noteworthy that cool unshocked ridges can be seen in Fig. 2a directly abutting the warm post-shock subshell in the south and west. Since these ridges have not yet been encountered by the SNR shock, as indicated by the lack of high velocity gas, they must pre-date the supernova event.

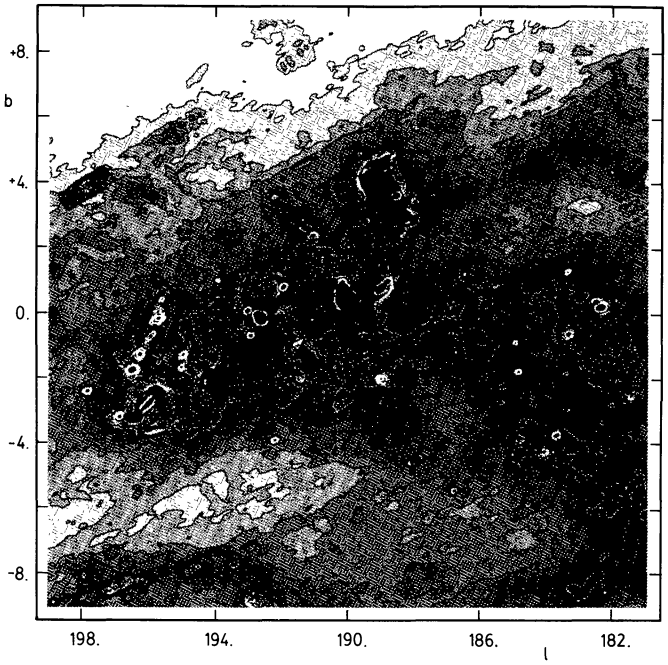

Fig. 9. The galactic anti-center at 100 μm. An 18° square field centered at $l = 190°$, $b = 0°$ illustrating the large scale environment of the IC 443 complex at $l = 189°$, $b = +3°$

Table 2. Stellar identifications

Designation [a]	Name	Spectral type	Distance modulus
a	HD 44139	B0.5 V	10.70
b	HD 43078	B0 IV	11.13
c	HD 254577	B0.5 II–III	11.01
d	HD 43582	B0 III	10.69
e	HD 254755	O9 Vp	10.41
f	HD 256035	O9 Vp	10.88
g	HD 43753	B0.5 III	11.06
h	HD 255055	O9 Vp	11.97
i	HD 43818	B0 II	10.95
j	HD 43384	B3 Iab	10.79
k	HD 254042	B0.5 IVnn	11.34
1	AGK 3 +22 685	(B8)	–
2	AGK 3 +22 686	(B3)	–

[a] With reference to Fig. 10
( ) Uncertain classification

A molecular component is also associated with the complex. A CO cloud ($V_{lsr} = -5\,km\,s^{-1}$) has been partially mapped by Scoville et al. (1977) and Cornett et al. (1977) extending across the center of IC 443 and continuing north-east to the position of the compact IR source at $\alpha = 6^h15^m30^s$, $\delta = 23°20'$. The appearance of this compact source is suggestive of a pre-main sequence molecular outflow. This is the only indication for ongoing star formation in this area. Compact ridges and peaks are also found in the CO distribution associated with the brightest accelerated H I. DeNoyer (1979) has found OH and ^{12}CO with velocities as large as $-60\,km\,s^{-1}$ while White (1985) has detected ^{12}CO out to $-80\,km\,s^{-1}$. Current treatments of shocks in molecular gas (Hollenbach and McKee, 1979, 1980) do not predict survival of CO with shock velocities $>40\,km\,s^{-1}$. Acceleration of the CO to the observed velocity might be accomplished by 1) more effective grain shielding of the molecules and/or faster cooling (than assumed by Hollenbach and McKee) behind a $\sim 75\,km\,s^{-1}$ shock or 2) ram pressure acceleration (McKee et al., 1978) of denser molecular clumps by a well coupled (i.e. dense) higher velocity neutral flow. In either case, a high shock ram pressure is indicated, $\varrho v^2 \sim 4\ 10^{-8}\,dyn\,cm^{-2}$, since the hydrogen density in the molecular gas must be $>300\,cm^{-3}$.

X-ray observations of IC 443 have revealed an amorphous emitting volume apparently filling much of the region bounded by bright optical filaments (Watson et al., 1983). The brightest emission is associated with the north of subshell *A*, while this entire region has higher surface brightness than subshell *B*. Faint emission extends beyond the eastern edge of the bright radio/optical emission of subshells *A* and *B*. The X-ray spectrum of IC 443 (Malina et al., 1976) implies a relatively high temperature $T = 2\ 10^6\,K$ and low pre-shock density $n_0 = 0.5\,cm^{-3}$. The corresponding pressure $1.5\ 10^{-8}\,dyn\,cm^{-2}$ is a factor ~ 3 less than that implied above for the high density shell.

A rather different view of the IC 443 complex is provided by the 327 MHz radio map shown in Fig. 5. As noted by previous authors (e.g. Duin and Van der Laan, 1975) most of the collisionally ionized optical filaments have bright radio synchrotron counterparts, while some of the remaining radio filaments are seen in neutral hydrogen (Braun and Strom, 1986a). Fainter, presumably thermal emission is associated with the region of diffuse ionized gas in the east, $\alpha = 6^h17^m$ to 6^h21^m and $\delta = 22°40'$ to $23°40'$, as well as the compact IR/CO source at $\alpha = 6^h15^m30^s$, $\delta = 23°20'$ (which we shall designate G 188.5+3.6). More intriguing is the large diameter partial shell structure which incorporates the north-east optical filaments (Fesen, 1984) and southern optical extension of IC 443 into parts of a more extended whole. A shell geometry is indicated by the well-defined outer boundary and more diffuse inner boundary of the semi-circular region of radio emission. It is also clear that the shell cavity of the large diameter shell (subshell *C* centered at $\alpha = 6^h16^m$, $\delta = 22°20'$ with diameter $\sim 85'$) is connected to that of IC 443. This is illustrated by the character of the optical filaments around the SNR periphery. While the outer edge is well defined in the north and along the entire western edge, the southern optical filaments (subshell *B*) of IC 443 join smoothly onto the large shell eastward of $\alpha = 6^h13^m$ (cf. Fig. 6b). The region of transition cannot be clearly seen in the north-east because subshell *A* continues partially around to the back face where it is seen in H I at velocities $V_{lsr} > +20\,km\,s^{-1}$ (e.g. Fig. 6c) before joining the larger shell. Recombined neutral hydrogen is also visible from the backside interface between subshells *B* and *C* at $V_{lsr} \sim +30\,km\,s^{-1}$ (Fig. 6d) over much of its length.

Thus, while the geometry is relatively complex, it is fully constrained by the available data. IC 443 consists of three interconnected roughly spherical subshells which have substantially different radii and centroids. It seems likely that this shell system is located near the rear of the cloud complex since the approaching subshell *A* is in contact with the CO cloud, while subshells *B* and *C* appear to be bounded by somewhat lower density ambient gas. The entire range of ionization conditions within post-shock gas appears to be represented; from 1) molecular and neutral atomic gas in the south of subshell *A* to 2) recombining atomic gas in the remainder of *A*, most of *B* and parts of *C*, and 3) the majority of subshell *C* which is likely to be at temperatures greater than 10^5 K.

3.2. *Physical parameters*

The atomic gas density [1] in the IC 443 complex can be estimated from the surface brightness of the cool dust component shown in Fig. 2a. The infrared spectrum of this component (nominal brightness ratios at 12:25:60:100 μm = 0.04:0.04:0.23:1.00) is similar except for the ubiquitous short wavelength excess) to that calculated by Draine and Anderson (1985) for a 3 times solar intensity radiation field. Under these conditions they predict a 100 μm (IRAS band) surface brightness normalized by the column density of $\sim 3.5\,MJy\,sr^{-1}\ 10^{20}\,cm^{-2}$. The plateau of cool dust emission underlying the complex has a 100 μm surface brightness of $\sim 25\,MJy\,sr^{-1}$, corresponding to a hydrogen column density $N_H \sim 7\ 10^{20}\,cm^{-2}$. Assuming a line-of-sight depth similar to the 25 pc (at $D = 1.5$ kpc) north-south extent results in a mean density estimate $n_H = 9\,cm^{-3}$. The loops and ridges in the central and eastern portions of the complex have 100 μm brightnesses of 40 to 70 $MJy\,sr^{-1}$ in excess of the plateau brightness, which corresponds to densities $n_H = 40$ to $100\,cm^{-3}$ assuming 6 to 10 pc depths. The cool compact ridges which are directly outside of the shocked front face of the SNR subshell *A* in the south and west have densities of at least $70\,cm^{-3}$ if a conservative 4 pc depth is assumed. However, if these features are distributed in a shell, as their appearance suggests, densities $n_H \sim 200\,cm^{-3}$ are implied.

The properties of the neutral and molecular components are in marked contrast to those of the diffuse photoionized gas. Integrated flux densities and source dimensions for S 249 and G 188.5+3.6, derived from the 327 MHz map of Fig. 5, are listed in Table 3 together with the physical parameters derived under the assumptions of a cylindrical geometry and 10^4 K electron temperature (following Mezger and Henderson, 1967; Hjellming, 1968). This gas is characterized by low electron densities; $n_e \sim 4\,cm^{-3}$ in the southern and northern halves of S 249 and only marginally higher (ionized) densities in G 188.5+3.6. The excitation parameter for S 249-S (south), $u = 31\,pc\,cm^{-2}$ is reasonably consistent with ionization by the apparently embedded O9 Vp star HD 256035, while that found for G 188.5+3.6, $u = 15\,pc\,cm^{-2}$ could be satified by an ionizing flux equivalent to that of a B0.5 V star (e.g. Churchwell and Walmsley, 1973). While no obvious candidate is apparent for the excitation of S 249-N (north) for which $u = 33\,pc\,cm^{-2}$, this could be provided by a small number of as yet unidentified early B stars or by HD 43818 (B0 II) and/or HD 255055 (O9 Vp) lying somewhat to the north-west (cf. Fig. 10).

The warm dust emission of Fig. 3 has also been used to constrain the properties of the H II regions. Integrated flux

[1] It must be remembered that any molecular component will be almost invisible to IRAS since the lower associated dust temperatures lead to both significantly lower intrinsic surface brightness and a spectral peak significantly longward of 100 microns

Table 3. Radio parameters of H II regions

	S 249-S	S 249-N	G 188.5+3.6
Flux density [Jy at 327 MHz]	3.7±0.4	4.5±0.5	0.40±0.04
Mean diameter [arcmin]	32.0	37.0	8.1
Electron density [cm^{-3}]	4.4	4.0	11.0
Ionized mass [$M_\odot$]	410.0	570.0	17.0
Emission measure [$pc\,cm^{-6}$]	280.0	260.0	480.0
Optical depth [10^{-3}]	1.0	0.8	1.6
Excitation parameter [$pc\,cm^{-2}$]	31.0	33.0	15.0

densities at 12, 25, 60, and 100 μm are listed in Table 4. The flux densities at 12 and 25 μm are significantly more uncertain due to contamination by remaining cool dust emission. The affected areas can be recognized by comparison with the derived cool dust distribution in Fig. 2a. These include the residual loop at $\alpha = 6^h19^m$, $\delta = 23°$ and the enhancement in the extreme north-east. Temperatures which we derive for these components will therefore be based on the flux densities at only 60 and 100 μm. In addition, it is clear that G 188.5+3.6 has been partially incorporated into the cool dust distribution. Fluxes for this source are therefore derived from the maps of Fig. 1. The 60/100 μm flux ratios have been simulated by integrating model spectra over the IRAS responsivity bands. The model spectra were based on a single temperature population of graphite and silicate grains using the absorption efficiencies of Draine and Lee (1984) as tabulated by Draine (1985). Virtually complete incorporation of solar abundance grain constituents is assumed, corresponding to a dust to gas ratio ~3% by mass. The derived grain temperatures and column density normalized surface brightnesses are listed in Table 4. If the same source dimensions and cylindrical geometry are assumed as for the radio continuum data, mean densities of $n_H < 1\,cm^{-3}$ are derived for S 249. However, it is clear from a comparison of Figs. 3 and 5 that the warm component of dust emission is more centrally concentrated than the diffuse thermal radio emission. Adopting these smaller dimensions yields densities $n_H \sim 3\,cm^{-3}$ in agreement with the electron density obtained from the radio data. It appears that the radiative heating of grains (to temperatures ~35 K) has only been effective out to about half the radius of significant photoionization.

The occurrence of such low densities within large volumes of the much higher density complex suggests that the action of stellar winds has partially evacuated regions of radius greater than the Stromgren radius around the respective stars so that only an amorphous circumstellar (wind enhanced) region becomes photoionized rather than the associated high density shell (cf. McKee et al., 1984). This process will be discussed further below.

The conditions in the vicinity of G 188.5+3.6 are clearly rather different. Even assuming that the radio dimensions apply to the region of dust emission implies a density $n_H = 240\,cm^{-3}$. However, as was the case with S 249, the warm dust emission appears to be more compact than the thermal radio nebula and is in this case unresolved (by the 6.'9 × 4.'6 beam). The implied densities, $n_H > 500\,cm^{-3}$ are consistent with the identification of this source with a compact CO peak (Cornett et al., 1977).

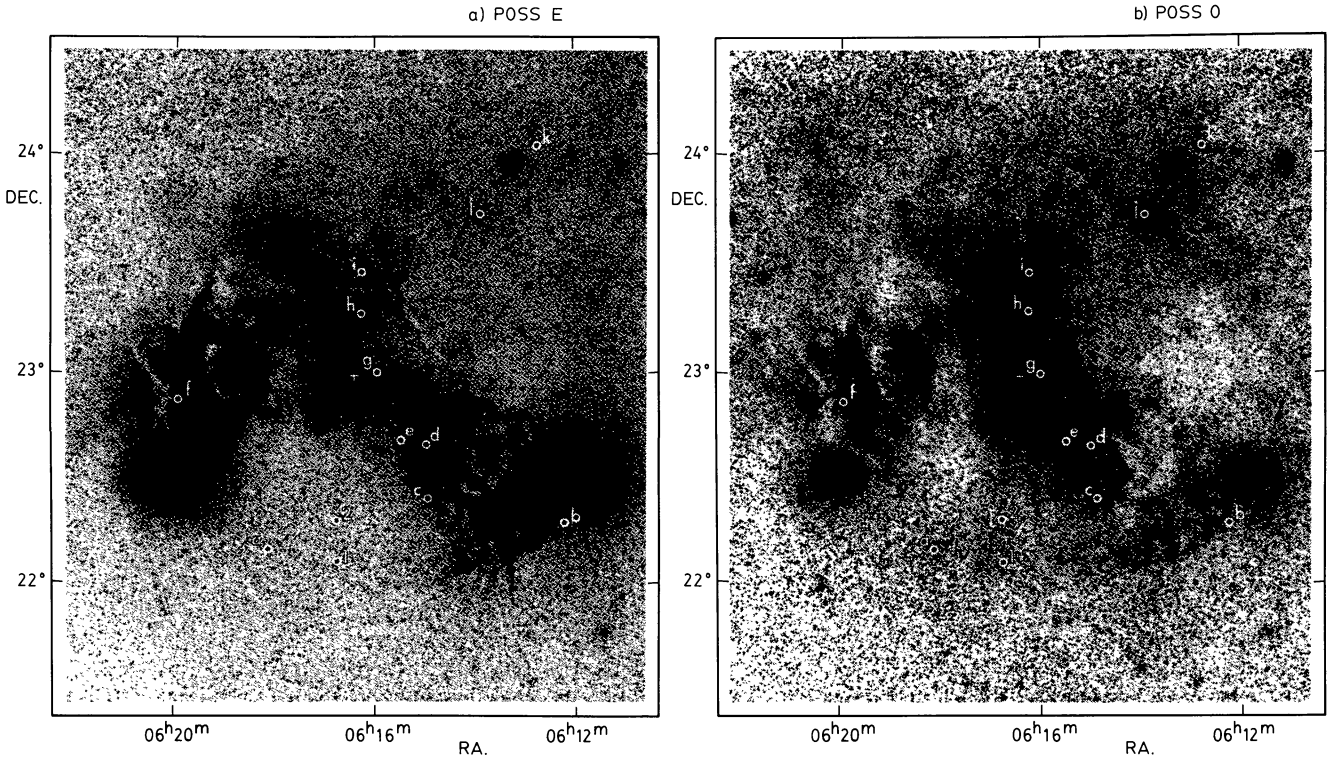

Fig. 10a and b. The optical appearance of the IC 443 complex, and location of Gem OB1 association members. The letter and number designations refer to Table 2

Table 4. Infrared parameters of H II regions

		S 249-S	S 249-N	G 188.5+3.6
Nominal flux density [Jy]	(12 μm)	(0.37)	(6.2)	68.0± 7.0
	(25 μm)	(47.0)	(46.0)	110.0± 10.0
	(60 μm)	375± 40	275± 30	1080± 110
	(100 μm)	540± 50	385± 40	2220± 220
Grain model temperature [K]		35.0	35.5	30.5
Surface brightness per H I Column density at 100 μm [MJy sr^{-1}/10^{20} cm^{-2}]		43.0	46.0	23.0
Mean radio diameter (θ_R) [arcmin]		32.0	37.0	8.1
Implied density (with θ_R) [cm^{-3}]		0.51	0.22	240.0
Mean infrared diameter (θ_{IR})		18.0	15.0	5.0
Implied density (with θ_{IR}) [cm^{-3}]		2.9	3.3	480.0

( ) Uncertain values

Examination of the warm dust images of IC 443 in Fig. 3 reveals substantial structural changes between the four wavelength bands, which apparently reflect local variations in the grain heating. The bright southern rim of subshell *A* dominates the 100 and 60 μm structure, while the north-eastern portion of the shell assumes prominence shortward of 25 μm. The expected emission from collisionally heated dust within shocked gas has been discussed by Draine (1981), with extensions and applications given by Braun (1986), Braun et al. (1986), and Braun and Strom (1986b). As discussed by Braun and Strom (1986b), a significant fraction of the shocked gas within optically bright SNR is likely to have recombined. This is especially apparent in IC 443 where post-shock H I, CO, OH, HCN, HCO^+, etc. are all observed along the bright southern rim mentioned above. Depending on the recombination time of the shocked gas, the grain population will have suffered some degree of processing. The emission spectrum of such recombined gas should be similar to that of the unshocked gas exposed to the same radiation field, although modified by a general decrease in grain radii due to sputtering and a diminished (very) small particle content due to catastrophic disruption and thermal sublimation. Since the recombination layer associated with moderate velocity shocks ($<200\,km\,s^{-1}$) has a thickness ~ 0.002 pc (Raymond, 1979), corresponding to 0.″3 at the distance of IC 443, the zones of shocked and recombined gas will not generally be spatially resolved.

However, before analyzing the collisionally heated gas component, its emission must be isolated. A reasonable decomposition of these components can be made in the case of IC 443 since a (bright) portion of the post-shock shell is quite clearly lacking high temperature gas. There are portions of the southern rim of subshell *A* where accelerated neutral atomic and molecular gas has no associated optical filaments (cf. Fig. 6b). The 60/100 μm ratio map shown in Fig. 11 illustrates that this same region also has the coolest apparent temperature ($T = 34$ K) occurring within the remnant. A similar ratio is found in diffuse portions of the extended complex suggesting that the local radiation field, perhaps

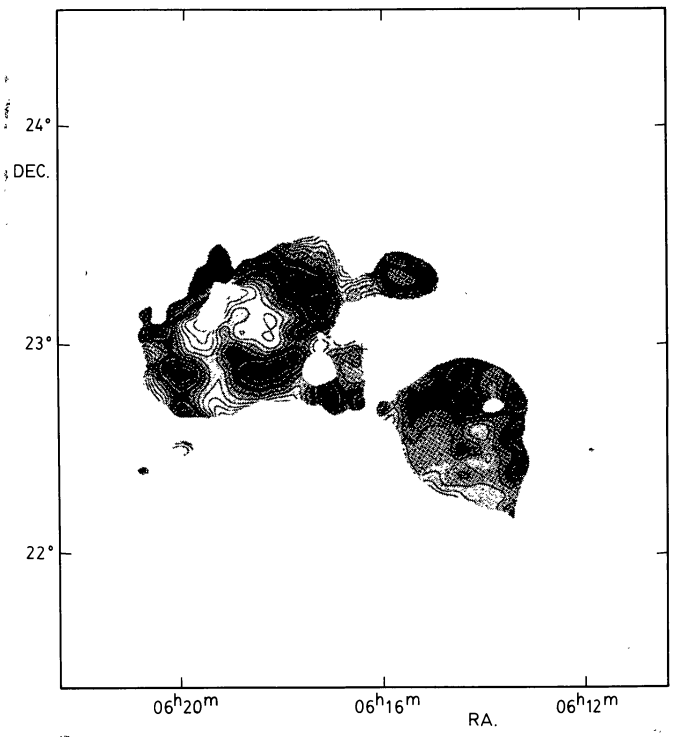

Fig. 11. The ratio of the 60/100 μm surface brightness in the background corrected warm dust images (Fig. 3c and d). The ratio was only defined were the 60 and 100 μm surface brightnesses were greater than 3.4 and 5.1 MJy/sr respectively. The grey scale is based on a histogram of map intensities. The linear contour levels are at 65 to 70 % in steps of 0.5 %

supplemented by that of IC 443 itself can sustain such temperatures within a relatively large volume. Braun (1986) has shown that the 25, 60, and 100 μm fluxes of collisionally heated dust are well fit by a single temperature grain model (as discussed above), while higher temperatures are generally evident in the 12 μm emission. We have therefore decomposed the integrated spectrum of IC 443 into one 34 K and one complementary temperature component constrained by the observed fluxes and the relative intensities of the model spectra in the 25, 60 and 100 μm bands. The unique complementary temperature which provides agreement with the observed spectrum is $T = 93.5 \pm 0.3$ K. The corresponding decomposed fluxes are listed in Table 1. Since the decomposition of the 12 μm flux is not defined by this procedure we will not consider it in the subsequent analysis. The model spectra were used to provide color corrections to the broad band IRAS fluxes as well as accurate estimates of the wavelength where the spectrum peaks, $\lambda_{\rm peak} = 27.5 \pm 1$ μm (in units of λI_λ) and the maximum surface brightness, $\lambda I_\lambda^{\max} = 2.45\ 10^{-7}$ W m^{-2} sr^{-1} for the shock-heated component within subshell *A*. These quantities are related to the local shock velocity, v_c, pre-shock density, n_c, current volume filling factor, f_c, and time since shock encounter, τ, by

$$\lambda I_\lambda^{\max} \simeq 6.96\ 10^{-6} f_c \left[16 \left(\frac{n_c \tau}{5\ 10^4}\right)^{1/2} - 15 \left(\frac{n_c \tau}{5\ 10^4}\right)\right] \cdot \left(\frac{n_c}{\rm cm^{-3}}\right)\left(\frac{v_c}{10^3\ {\rm km\ s^{-1}}}\right)^3 {\rm W\ m^{-2}\ sr^{-1}} \quad (1a)$$

for $n_c \tau < 5\ 10^3$ cm^{-3} yr, and $v_c \lesssim 1200$ km s^{-1}

$$\lambda I_\lambda^{\max} \simeq 3.48\ 10^{-5} f_c \left(\frac{n_c}{\rm cm^{-3}}\right)\left(\frac{v_c}{10^3\ {\rm km\ s^{-1}}}\right)^3 {\rm W\ m^{-2}\ sr^{-1}} \quad (1b)$$

for $n_c \tau > 10^4$ cm^{-3} yr, and

$$\lambda_{\rm peak} \simeq 37.6 \left(\frac{n_c}{\rm cm^{-3}}\right)^{-0.18} \left(\frac{v_c}{10^3\ {\rm km\ s^{-1}}}\right)^{-0.3} \mu{\rm m} \quad (2)$$

(Eqs. (3), (4) and (5) from Braun, 1986).

Since the decomposition of IC 443's integrated spectrum indicates only a 5% recombined contribution to the 25 μm image (Fig. 3b) this map provides a good indication of the brightness distribution of the shock-heated dust. The shock-heated dust is clearly well correlated with the bright optical filaments (cf. Fig. 6b) suggesting that a similar local shock velocity may apply. Both radial velocity studies (Lozinskaya, 1969; Pismis and Rosado, 1974) and optical spectroscopy (e.g. Fesen and Kirshner, 1980) indicate that the brightest optical filaments have shock velocities, $v_c = 70$ km s^{-1}. Equation 2 then yields a pre-shock density $n_c = 480$ cm^{-3}. Although this density appears uncomfortably high at first glance, there are a number of further indications to support it. As discussed in Sect. 3.1 the observation of CO accelerated to 75 km s^{-1} (White, 1985) implies a similar shock ram pressure if the acceleration mechanism is either direct blast wave acceleration (McKee and Cowie, 1975) or an efficient combination of blast wave and ram pressure acceleration (McKee et al., 1978). The optical spectra also give an indication that such pre-shock densities may be present. Fesen and Kirshner (1980; hereafter FK 80) conclude that their optical spectra most closely resemble the models BB and HH of Raymond (1979). Both of these models have depleted gas abundances (as would be expected with the dust content we observe) and shock velocities $v_c = 70.7$ km s^{-1} in agreement with the kinematic studies. However, model BB has a pre-shock density $n_c = 10$ cm^{-3} while model HH has a pre-shock density $n_c = 300$ cm^{-3}. Since relatively low post-shock electron densities are inferred by FK 80 from the [S II] 6716/6731 line ratios, $n_e = 300$ cm^{-3}, they suggest that a low pre-shock density is appropriate. However, the observed [S II] line intensities are not well matched by any of the slow (< 80 km s^{-1}) shock models of Raymond (including BB and HH) suggesting that the bulk of [S II] emission may originate in higher velocity shocks within lower density gas along the line of sight. Given the short recombination times appropriate for pre-shock densities $n_c = 480$ cm^{-3} ($\tau \simeq 10$ yr, cf. Raymond, 1979) the usual (equilibrium) assumptions inherent in the density determination technique may also not be appropriate.

A more direct estimate of the shock ram pressure can be made from the H_β surface brightnesses observed by FK 80, through comparison with those predicted by the models of Raymond (1979). Since the optical filamentary system is complex, each slit position is likely to sample a number of recombination layers along the line of sight. The least confused position (FK 80 #3) also has one of the lowest observed H_β surface brightnesses $I_\lambda = 2.0\ 10^{-7}$ W m^{-2} sr^{-1}. Scaling the surface brightness of model HH ($n = 300$ cm^{-3}) linearly with density (as suggested by Raymond, 1979) to $n_c = 480$ cm^{-3} results in a predicted surface brightness $I_\lambda = 1.4\ 10^{-7}$ W m^{-2} sr^{-1} in reasonable agreement with the observed value. Model BB on the other hand predicts a surface brightness, $I_\lambda = 3.0\ 10^{-9}$ W m^{-2} sr^{-1}; almost two orders of magnitude fainter than that observed.

The X-ray derived ram pressure ($\sim 1.5\ 10^{-8}$ dyn cm^{-2}) provides further evidence for the existence of high pressures within IC 443. The amorphous appearance of the X-ray emission suggests that this pressure should be representative of a thick zone within the SNR interior. The pressure ratio we find between the bright filaments and the X-ray interior, $F = n_c v_c^2 / n_x v_x^2 = 3.5$ is similar to the maximum pressure ratio $F = 3.15$ predicted by McKee and Cowie (1975) to occur under just such conditions of high density contrast.

The current volume filling factor for the high density gas within subshell *A* can be calculated from equation 1a (with $\tau = 10$ yr) yielding $f_c = 0.06$. If the pre-SN gas had been uniformly clumpy with this filling factor, the mass of high density shocked gas would be

$$M_c = f_c \tfrac{4}{3} \pi r^3 \mu m_{\rm H} n_c = 740\ M_\odot$$

(with a mean molecular weight, $\mu = 1.3$ and radius $r = 5.8$ pc) while the kinetic energy imparted to the ISM

$$E_k^{\rm ISM} = \tfrac{1}{2} M v^2 = \tfrac{1}{2} (\tfrac{4}{3} \pi r^3 \mu m_{\rm H} n_c)\ (\beta v_c)^2 = 0.0450 \left(\frac{r}{2\ {\rm pc}}\right)^3 \left(\frac{n_c}{\rm cm^{-3}}\right)\left(\frac{v_c}{10\ {\rm km\ s^{-1}}}\right)^2 10^{50}\ {\rm erg} \quad (3)$$

$$= 2.6\ 10^{50}\ {\rm erg}$$

[assuming approximate pressure equilibrium and $\sim$adiabatic post-shock velocity and density profiles to yield $\beta = 0.647$, cf. Braun (1986)]. If the current intercloud shock is approximately adiabatic, the initial energy of the SN would have been (Chevalier, 1974) $E_0 = E_k^{\rm ISM}/0.283 = 9.1\ 10^{50}$ erg. As also concluded by Braun and Strom (1986b) in regard to the Cygnus Loop, the factor of ~ 4 excess energy over young SNR (e.g. Braun, 1986) which follows from the uniform mean density assumption is most reasonably resolved by adopting a pre-SN shell geometry. As already discussed above, the cool dust "ridges" which border the shocked and recombined gas in the south of subshell *A* are a strong indication for a pre-SN high density shell in this portion of the complex. It is also clear that subshell *C* and perhaps subshell *B*

were initially formed by independent processes. Assuming a shell geometry, the mass of the shocked ISM within subshell A is

$$M_c = f_c 4\pi r^2 \Delta r \mu m_H n_c = 200\, M_\odot$$

with an estimated (shocked) shell thickness $\Delta r = 0.5$ pc (cf. Fig. 7a and below), while the kinetic energy of shocked ISM is

$$E_k^{ISM} = \tfrac{1}{2} M v^2 = \tfrac{1}{2}(4\pi r^2 \Delta r \mu m_H n_c)\,(\beta v_c)^2$$

$$= 0.019 \left(\frac{r}{10\,\mathrm{pc}}\right)^2 \left(\frac{r}{\mathrm{pc}}\right)\left(\frac{n_c}{\mathrm{cm}^{-3}}\right)\left(\frac{v_c}{10^2\,\mathrm{km\,s}^{-1}}\right)^2 10^{50}\,\mathrm{erg} \quad (4)$$

$$= 0.67\ 10^{50}\,\mathrm{erg}$$

so that $E_0 = 2.4\ 10^{50}$ erg, which is in reasonable agreement with the mean value of $E_0 = 1.6\ 10^{50}$ erg found for Tycho, Kepler and Cas A (Braun, 1986). If an initial shock velocity of $v_s = 12{,}000$ km s^{-1} is assumed with $\sim$ adiabatic internal density and velocity profiles, the associated mass of ejecta given by $E_0 = 0.209\, M_0 v_s^2$ (cf. Braun, 1986) is $M_0 = 0.4\, M_\odot$.

Such a geometry also allows a consistent interpretation of the neutral hydrogen data. The position-velocity cut through the H I data in Fig. 7 illustrates the increase in apparent velocity width of emission features which are closest to the center of subshell A. While the largest radial velocities are indeed found toward this position, closer inspection of the emission features of high velocity width reveals that they often vary systematically in position as a function of velocity, leading to slightly skewed ridges of emission in position-velocity maps. This "skewing" of the emission ridges does not occur systematically out (to larger radii at larger velocities) or in (as might be expected for a geometrical effect) but is apparently associated with the properties of individual clouds and filaments. The clearest example of this phenomenon is given by the cloud shown in Fig. 8. A relatively compact core is seen at a velocity of -20 km s^{-1}, which becomes increasingly extended, divides into multiple subpeaks and forms an incomplete ring before disappearing at -100 km s^{-1}. The position-velocity map at fixed declination through the center of the cloud shown in Fig. 8b illustrates the velocity "skewing" to both the east and west of the low velocity core, although as seen in Fig. 8a this actually occurs in almost all directions with respect to the cloud core. The physical linewidths within a small volume of gas must therefore be much narrower than the overall width found for a given feature. The simplest explanation for this phenomenon appears to be a density gradient in the pre-shock clouds and filaments which leads to a velocity gradient after shock passage, combined with fortuitous geometry which provides spatial separation. The cloud of Fig. 8 appears to have a high density core and more tenuous mantle such as might reasonably be expected. Examination of the available examples of skewed emission ridges yields the following estimates of average properties. Low velocity cores have (isothermal) shock velocities $v_s^A \sim 15$ km s^{-1} (with respect to $V_{lsr} \sim -5$ km s^{-1}), (projected apparent) velocity dispersions $\sigma_T^A \sim 8$ km s^{-1} and H I brightness temperature $T_B^A \sim 25$ K, while the high velocity features have shock velocity $v_s^B \sim 75$ km s^{-1}, velocity dispersions $\sigma_T^B \sim 16$ km s^{-1} and H I brightness temperature $T_B^B \sim 7$ K. Pre-shock densities appropriate for these shock velocities can be calculated under the assumption of pressure equilibrium, yielding $n_H^A = 10{,}500$ cm^{-3} and $n_H^B = 420$ cm^{-3}. Assuming a (partial) shell geometry, the maximum face-on optical depth in the $\lambda 21$ cm line can be written as

$$\tau_{HI} = 0.69 \left(\frac{n_H}{100\,\mathrm{cm}^{-3}}\right)\left(\frac{v_s}{100\,\mathrm{km\,s}^{-1}}\right)\left(\frac{t}{10^4\,\mathrm{yr}}\right) \cdot \left(\frac{\sigma_T}{10\,\mathrm{km\,s}^{-1}}\right)^{-1}\left(\frac{T}{10\,\mathrm{K}}\right)^{-1} \quad (5)$$

with t the time since shock encounter of the (rapidly recombining) high density shell of pre-shock density n_H and isothermal shock velocity v_s, which has a post-recombination temperature T and velocity dispersion σ_T. The observed brightness temperature is given as usual by

$$T_B = T(1 - e^{-\tau}).$$

After recombination, the post-shock gas should cool rapidly at the densities under consideration to an equilibrium temperature which is governed primarily by heating due to H_2 formation on grains,

$$\Gamma_{Hd} = 2.2\ 10^{-28} z_H n_H n(\mathrm{H\,I})\,\mathrm{erg\,cm}^{-3}\,\mathrm{s}^{-1} \quad (6)$$

(with z_H = the fraction of the binding energy of molecule formation which goes into translational kinetic energy) and cooling due to collisional excitation of ions (predominantly C II) by H I (Spitzer, 1978)

$$\Lambda_{HCII} = 7.9\ 10^{-27} n_H^2 d_c e^{-92.0/T}\,\mathrm{erg\,cm}^{-3}\,\mathrm{s}^{-1} \quad (7)$$

in which d_c is the fractional depletion of Carbon $(n_c/n_H)/(n_c/n_H)_{Solar}$. Since both of these rates are proportional to the density squared, the equilibrium temperature will be independent of density to first order. Equating the heating and cooling rates yields,

$$T = \frac{92.0}{\ln(36.0\, d_c/z_H)}\ \mathrm{K} \quad (8)$$

The fractional depletion of carbon we have assumed in the grain model for analysis of the dust emission is $d_c = 0.5$. The appropriate value of z_H is considerably less certain, with estimates in the range $z_H = 0.1$ to 1.0 (Spitzer, 1978). Adopting $z_H = 0.5$ yields a temperature $T = 26$ K from Eq. (8).

Since parameter estimates exist for the H I emission under two sets of conditions, the kinematic temperature of the gas can be independently derived from the observations. Assuming the same time since shock encounter, t, and kinetic temperature, T, the ratio of optical depths, γ, can be derived from Eq. 5, $\gamma = \tau^A/\tau^B = 10$. The ratio of brightness temperature $T^A/T^B = 25/7$ can then be used with

$$\frac{T^A}{T^B} = \frac{(1 - \exp(-\gamma\tau^B))}{(1 - \exp(-\tau^B))}$$

to determine the optical depths $\tau^A = 3.1$ and $\tau^B = 0.31$, which correspond to a kinetic temperature $T = 26$ K, in agreement with the estimate above.

The feasibility of powering the entire multi-cavity system with a single SN blast wave can now be assessed by considering the time since shock encounter for the high density shell. The above parameters together with Eq. (5), yield $t = 6000$ yr. Since the eastern edge of subshell C lies ~ 25 pc beyond the edge of subshell A, a mean velocity $\langle v_s \rangle = 4070$ km s^{-1} is required for the shock to have reached this position. This implies that a relatively small ratio of swept-up to ejected mass,

$$X \equiv 4\pi r^3 \mu m_H n_H / (3\, M_0) \quad (10)$$

has been reached locally. The shock radius for intermediate (pre-adiabatic) mass ratios $0.05 < X < 17.0$ evolves with time approximately as

$$r_s = v_0 (0.75 - 0.127 \log^2 X) X^{-0.195} t \quad (11)$$

(cf. Braun, 1986). Assuming an initial shock velocity $v_0 = 12{,}000$ km s^{-1}, allows calculation of the mass ratio $X = 15$ via Eq. (11).

The ejecta mass derived above, $M_0 = 0.4\,M_\odot$ then implies a density within the cavity of $n = 0.003\,\mathrm{cm}^{-3}$ via Eq. 10. The shock velocity on reaching the edge of subshell C is given by (cf. Braun, 1986)

$$v_s = v_0\,(0.75 - 0.127 \log^2 X)\,X^{-0.338} = 2800\,\mathrm{km\,s}^{-1} \tag{12}$$

The above parameters are clearly reasonable, although a relatively low cavity density is implied.

Since the H I kinetic temperature derived above is likely to be representative for such recombined gas, let us consider under what conditions Eq. (5) predicts observable quantities of accelerated H I. Taking $T = 25\,\mathrm{K}$, $\sigma_T = 10\,\mathrm{km\,s}^{-1}$, $t = 5000\,\mathrm{yr}$ and $v_s = 50\,\mathrm{km\,s}^{-1}$, a brightness temperature $T_B > 2\,\mathrm{K}$ requires pre-shock densities $n_\mathrm{H} > 100\,\mathrm{cm}^{-3}$. If an SNR were expanding in a medium of mean density $n_\mathrm{H} = 100\,\mathrm{cm}^{-3}$, its radius would be limited to $< 5\,\mathrm{pc}$. The observation of extensive accelerated H I emission in a large diameter SNR is therefore already a fairly clear indication for a pre-SN shell geometry. Since extensive accelerated H I has been found associated with each of the four large diameter SNR searched with high sensitivity by Braun and Strom (1986a) (IC 443, VRO 42.05.01, CTB 109 and G78.2+2.1) it seems likely that the general nature of the associated H I phenomenon reflects the general nature of the pre-SN shell phenomenon.

The important conclusion of Sect. 3.1 was that IC 443 is composed of not one, but three interconnected roughly spherical cavities. The observed brightness distribution was shown above to be consistent with excitation of the entire system by a single SN blast wave centered within subshell A, which propagates rapidly in the low density cavity before encountering the high density walls. The obvious question is, what has given rise to this multiple cavity? The most likely answer is, the massive stars of the Gem OB1 association. The creation of stellar wind blown bubbles has been considered by a number of authors; most recently by Weaver et al. (1977) and McKee et al. (1984). The occurrence, of such structures is a natural consequence of stellar evolution in a moderate density environment. Photo-evaporation will tend to homogenize an initially cloudy medium of mean density n_m out to a radius

$$R_h\,(t_\mathrm{ms}) = 56\,n_m^{-0.3}\,\mathrm{pc} \tag{13}$$

during the main sequence lifetime

$$t_\mathrm{ms} = 4.4\ 10^6 \left(\frac{N_i}{10^{49}}\right)^{-1/4}\,\mathrm{yr} \tag{14}$$

of a B0 or earlier star emitting N_i ionizing photons per second (McKee et al., 1984). The stellar wind will sweep a dense shell from the homogenized region and leave a low density bubble around the star. While the shell evolves within the homogenized region it will have radius

$$R_b\,(t) = 27\,n_m^{-1/5} \left(\frac{L_W}{10^{36}\,\mathrm{erg}}\right)^{1/5} \left(\frac{t}{10^6\,\mathrm{yr}}\right)^{3/5}\,\mathrm{pc} \tag{15}$$

for a stellar wind luminosity

$$L_W = 1.2\,M_W v_W^2 = 1.27 \cdot \left(\frac{\dot{M}_W}{10^{-6}\,M_\odot\,\mathrm{yr}^{-1}}\right) \left(\frac{v_W}{2000\,\mathrm{km\,s}^{-1}}\right)^2 10^{36}\,\mathrm{erg\,s}^{-1} \tag{16}$$

(Castor et al., 1975). Upon reaching the homogenization radius further expansion will be primarily constrained by the rate of growth of the homogenization radius (McKee et al., 1984)

$$R_h\,(t) = 1.05 \left(\frac{t}{t_\mathrm{St}}\right)^{4/7} R_\mathrm{St}, \tag{17}$$

$$R_\mathrm{St} = 66.9\,n_m^{-2/3} \left(\frac{N_i}{10^{49}}\right)^{1/3}\,\mathrm{pc}, \tag{18}$$

$$t_\mathrm{St} = 6.5\ 10^6\,n_m^{-2/3} \left(\frac{N_i}{10^{49}}\right)^{1/3}\,\mathrm{yr} \tag{19}$$

The large subshell C has radius $r = 19\,\mathrm{pc}$ and is situated in the southern rear portion of the complex where ambient densities are of order $10\,\mathrm{cm}^{-3}$. At least three B stars are seen near the center of subshell C; HD 44139, AGK 3 +22 685 and AGK 3 +22 686 (cf. Fig. 10). Only HD 44139 has a well determined spectral type; B0.5 V. Its distance modulus is within 0.2 mag of that for HD 256035 which we identified as the exciting star for S 249-S, placing it in the vicinity of the complex. Typical values for a B0.5 V star are a mass loss rate $\dot{M}_W = 4.6\ 10^{-8}\,M_\odot\,\mathrm{yr}^{-1}$ (Lamers, 1981), wind velocity $v_w = 2700\,\mathrm{km\,s}^{-1}$ (Abbott, 1978) and $N_i = 3.2\ 10^{46}\,\mathrm{s}^{-1}$ (Panagia, 1973). Assuming a uniform initial density $n \sim 10\,\mathrm{cm}^{-3}$, a single B0.5 V star will evacuate a bubble of radius 19 pc in $3.8\ 10^6\,\mathrm{yr}$ via Eq. (15); only 20% of its main sequence lifetime. However, if the environment is cloudy, radiative cooling during filament formation in the shell will limit the bubble radius to the homogenization radius. The time required to evacuate the 19 pc subshell under such conditions is $t = 9\ 10^6\,\mathrm{yr}$ [via Eq. (17)], i.e. still only 50% of a B0.5 star's main sequence lifetime. If HD 44139 is the only star powering subshell C and is approaching the end of its main sequence lifetime the mean initial density can be estimated from Eq. (13) yielding $n_m = 40\,\mathrm{cm}^{-3}$. Assuming a 10% shell thickness, $\Delta r = 1.9\,\mathrm{pc}$ implies mean shell densities of $n_m = 70$ to $270\,\mathrm{cm}^{-3}$ for initial densities of $n_m = 10$ to $40\,\mathrm{cm}^{-3}$ respectively. If additional early B stars were involved in powering the subshell or if there were a significant contribution from the adjoining subshells A/B, higher initial and shell densities would be implied.

No convincing candidate for the evacuation of subshell B has yet been identified, although the high absorption near its geometrical center limit the sensitivity of current studies. As a working hypothesis we will consider the action of a single star of type O in shaping both subshells A and B before its disruption in the SN event. The mean radius of the homogenized wind blown bubble of which the inner surface is currently being shocked is $R_h = 12\,\mathrm{pc}$. Equation 14 then yields a mean initial density $n_m = 170\,\mathrm{cm}^{-3}$. Assuming a 10% shell thickness, $\Delta r = 1.2\,\mathrm{pc}$ yields a mean shell density $n = 490\,\mathrm{cm}^{-3}$, in good agreement with the pre-shock density implied by the shock-heated dust spectrum. Mean densities are likely to be considerably higher within the compact southern rim of subshell A.

The observation of amorphous X-ray emission from subshells A and B suggests that the typical densities within these cavities are a few tenths (cf. Malina et al., 1976) in contrast to the more tenuous gas apparently within subshell C. The location of the bright X-ray region in the north of subshell A is interesting in that this represents the most nearly complete (hemi-)spherical subshell of small radius. It seems likely that the enhanced X-ray emission is due to slow ($\sim 1000\,\mathrm{km\,s}^{-1}$) ejecta which has been intercepted by a reasonably well-focused reverse shock, since only a small mass ($\sim 0.4\,M_\odot$) of high velocity ejecta appears to be driving the blast wave.

4. Conclusion

A consistent analysis has emerged of the physical parameters and processes occurring within a stellar association of intermediate age. Massive stars condensing from the molecular cloud soon begin returning mass and energy to the system via stellar winds. While the early stages of environmental processing are illuminated by

photoionization, the wind-blown bubble radius soon exceeds the photoionization radius leaving much of the resulting structure invisible. The explosive mass and energy injection of a SN provides a brief period of acceleration, compression and illumination of the processed environment; revealing and modifying the intricate system of interconnected shells.

Most stages of stellar/ISM evolution are visible within the IC 443 complex. The pre-main sequence IR/CO source G188.5 +3.6 has only recently begun shedding its high density cocoon. The O9 Vp star HD 256035, on the other hand, has apparently partially evacuated a low density bubble from the surrounding cloud. The star's ionizing flux is only sufficient to photoionize the central, wind-enriched core of the bubble. One or more of the stars: HD 44139, AGK 3 +22 685 and AGK 3 +22 686 have spent much of their main sequence lifetime in evacuating the large diameter bubble (subshell *C* of Sect. 3.1); while a single star of type O would have had sufficient wind energy to evacuate the smaller double shell (subshells *A* and *B*) before exploding in an SN event and shocking the entire three subshell IC 443 system.

The existence of a pre-SN shell was also implied for the Cygnus Loop (Braun and Strom, 1986b) by a large body of observational evidence. Since a number of the characteristics which suggest a pre-SN shell are shared by most forbidden line SNR (1. a systematic radial increase in ionization state and 2. an apparent implied initial energy – diameter dependence), Braun and Strom (1986b) conclude that this is a very general phenomenon. A further indication for generality comes from the observation of extensive, accelerated H I in each of the evolved SNR thus far observed with sufficient sensitivity (Braun and Strom, 1986a). The current source diameter and filling factor of high pre-shock density gas implied by the detection of recombined H I is a strong indication of a pre-SN shell geometry.

The lack of confusion in the direction of the IC 443 complex and the great variety of ongoing physical processes have allowed us to illustrate the consistency of the stellar wind blown bubble scenario (Weaver et al., 1977; McKee et al., 1984) in generating pre-SN shells. Since only stars of (main sequence) spectral type mid-B or earlier have sufficient wind energies to drive shells, the accompanying supernova events will be of type II. Such SNR should be found within ~100 pc of their birth sites (excepting high peculiar velocity pre-cursers which could also lead to more bizarre SNR morphologies as seen in G 357.7 − 0.1 and G 5.3 − 1.0, Becker and Helfand, 1985) and should often be associated with molecular clouds and the H II regions of fellow association members.

Acknowledgements. RB acknowledges the financial support of the Netherlands Foundation for Astronomical Research (ASTRON). The Westerbork Synthesis Radio Telescope is operated by the Netherlands Foundation for Radio Astronomy (SRZM). Both Foundations are supported by the Netherlands Organization for the Advancement of Pure Research (Z.W.O.).

References

Abbott, D.C.: 1978, *Astrophys. J.* **225**, 893
Becker, R.H., Helfand, D.J.: 1985, *Nature* 313, 115
Bos, A., Raimond, E., van Someren Greve, H.W.: 1981, *Astron. Astrophys.* **98**, 251
Braun, R.: 1986, *Astron. Astrophys.* (in press)
Braun, R., Walterbos, R.A.M.: 1985, *Astron. Astrophys.* **143**, 307
Braun, R., Strom, R.G.: 1986a, *Astron. Astrophys. Suppl.* (in press)
Braun, R., Goss, W.M., Caswell, J.L., Roger, R.S.: 1986, *Astron. Astrophys.* (in press)
Braun, R., Strom, R.G.: 1986b, *Astron. Astrophys.* (submitted)
Castro, J., McCray, R., Weaver, R.: 1975, *Astrophys. J.* **200**, L107
Chevalier, R.A.: 1974, *Astrophys. J.* **188**, 501
Churchwell, E., Walmsley, C.M.: 1973, *Astron. Astrophys.* **23**, 117
Cornett, R.H., Chin, G., Knapp, G.R.: 1977, *Astron. Astrophys.* **54**, 889
DeNoyer, L.K.: 1977, *Astrophys. J.* **212**, 416
DeNoyer, L.K.: 1979, *Astrophys. J.* **232**, L165
Draine, B.T.: 1981, *Astrophys. J.* **245**, 880
Draine, B.T.: 1985, *Astrophys. J. Suppl.* **57**, 587
Draine, B.T., Lee, H.M.: 1984, *Astrophys. J.* **286**, 89
Draine, B.T., Anderson, N.: 1985, *Astrophys. J.* **292**, 494
Duin, R.M., Van der Laan, H.: 1975, *Astron. Astrophys.* **40**, 111
Erickson, W.C., Mahoney, M.J.: 1985, *Astrophys. J.* **290**, 596
Fesen, R.A., Kirshner, R.P.: 1980, *Astrophys. J.* **242**, 1023
Fesen, R.A.: 1984, *Astrophys. J.* **281**, 658
Hjellming, R.M.: 1968, *Astrophys. J.* **154**, 533
Hollenbach, D., McKee, C.F.: 1979, *Astrophys. J. Suppl.* **41**, 555
Hollenbach, D., McKee, C.F.: 1980, *Astrophys. J.* **241**, L47
Humphreys, R.M.: 1978, *Astrophys. J. Suppl.* **38**, 309; Israel, F.P.: 1976, *Astron. Astrophys.* **52**, 175
IRAS Explanatory Supplement: 1985, eds. C.A. Beichman, G. Neugebauer, H.J. Habing, P.E. Clegg, T.J. Chester
Lamers, H.J.G.L.M.: 1981, *Astrophys. J.* **225**, 893
Locke, J.L., Galt, J.A., Costain, C.H.: 1964, *Astrophys. J.* **139**, 3
Lozinskaya, T.A.: 1969, *Soviet Astr. AJ* **13**, 192
Malina, R., Lampton, M., Bowyer, S.: 1976, *Astrophys. J.* **147**, 471
McKee, C.F., Van Buren, D., Lazareff, B.: 1984, *Astrophys. J. Letters* **278**, L115
Panagia, N.: 1973, *Astron. J.* **78**, 929
Pismis, P., Rosado, M.: 1974, *Rev. Mexicana Astron. Astrophys.* **1**, 121
Raymond, J.C.: 1979, *Astrophys. J. Suppl.* **39**, 1
Scoville, N.Z., Irvine, W.M., Wannier, P.G., Predmore, C.R.: 1977, *Astrophys. J.* **216**, 320
Spitzer, L., Jr.: 1978, Physical Processes in the Interstellar Medium, Wiley, New York
Van Albada, G.D., Baud, B., Boulanger, F., De Pagter, P., Pol, W., Renes, J.J., Wesselius, P.R.: 1984, Internal Report ROG, IRAS Splines I
Watson, M.G., Willingale, R., Pye, J.P., Rolf, D.P., Wood, N., Thomas, N., Seward, F.: 1983, in *Supernova Remnants and their X-ray Emission*, eds. J. Danziger, P. Gorenstein, Reidel, Dordrecht
Weaver, R., McCray, R., Castor, J., Shapiro, P., Moore, R.: 1977, *Astrophys. J.* **218**, 377
White, G.: 1985 (private communication)